remote sensing

MDPI

Article

Detecting the Responses of CO_2 Column Abundances to Anthropogenic Emissions from Satellite Observations of GOSAT and OCO-2

Mengya Sheng [1,2], Liping Lei [1], Zhao-Cheng Zeng [3,4,*], Weiqiang Rao [1,2] and Shaoqing Zhang [1,2]

[1] Key Laboratory of Digital Earth Science, Aerospace Information Research Institute, Chinese Academy of Sciences, Beijing 100094, China; shengmy@radi.ac.cn (M.S.); leilp@radi.ac.cn (L.L.); raowq@radi.ac.cn (W.R.); zhangshq@radi.ac.cn (S.Z.)

[2] University of Chinese Academy of Sciences, Beijing 100049, China

[3] Joint Institute for Regional Earth System Science & Engineering (JIFRESSE), University of California, Los Angeles, CA 90095, USA

[4] Division of Geological and Planetary Sciences, California Institute of Technology, Pasadena, CA 91125, USA

* Correspondence: zcz@gps.caltech.edu

Abstract: The continuing increase in atmospheric CO_2 concentration caused by anthropogenic CO_2 emissions significantly contributes to climate change driven by global warming. Satellite measurements of long-term CO_2 data with global coverage improve our understanding of global carbon cycles. However, the sensitivity of the space-borne measurements to anthropogenic emissions on a regional scale is less explored because of data sparsity in space and time caused by impacts from geophysical factors such as aerosols and clouds. Here, we used global land mapping column averaged dry-air mole fractions of CO_2 (XCO_2) data (Mapping-XCO_2), generated from a spatio-temporal geostatistical method using GOSAT and OCO-2 observations from April 2009 to December 2020, to investigate the responses of XCO_2 to anthropogenic emissions at both global and regional scales. Our results show that the long-term trend of global XCO_2 growth rate from Mapping-XCO_2, which is consistent with that from ground observations, shows interannual variations caused by the El Niño Southern Oscillation (ENSO). The spatial distributions of XCO_2 anomalies, derived from removing background from the Mapping-XCO_2 data, reveal XCO_2 enhancements of about M due to anthropogenic emissions and seasonal biomass burning in the wintertime. Furthermore, a clustering analysis applied to seasonal XCO_2 clearly reveals the spatial patterns of atmospheric transport and terrestrial biosphere CO_2 fluxes, which help better understand and analyze regional XCO_2 changes that are associated with atmospheric transport. To quantify regional anomalies of CO_2 emissions, we selected three representative urban agglomerations as our study areas, including the Beijing-Tian-Hebei region (BTH), the Yangtze River Delta urban agglomerations (YRD), and the high-density urban areas in the eastern USA (EUSA). The results show that the XCO_2 anomalies in winter well capture the several-ppm enhancement due to anthropogenic CO_2 emissions. For BTH, YRD, and EUSA, regional positive anomalies of 2.47 ± 0.37 ppm, 2.20 ± 0.36 ppm, and 1.38 ± 0.33 ppm, respectively, can be detected during winter months from 2009 to 2020. These anomalies are slightly higher than model simulations from CarbonTracker-CO_2. In addition, we compared the variations in regional XCO_2 anomalies and NO_2 columns during the lockdown of the COVID-19 pandemic from January to March 2020. Interestingly, the results demonstrate that the variations of XCO_2 anomalies have a positive correlation with the decline of NO_2 columns during this period. These correlations, moreover, are associated with the features of emitting sources. These results suggest that we can use simultaneously observed NO_2, because of its high detectivity and co-emission with CO_2, to assist the analysis and verification of CO_2 emissions in future studies.

Keywords: Mapping XCO_2; anthropogenic emission; GOSAT; OCO-2; NO_2 columns

check for updates

Citation: Sheng, M.; Lei, L.; Zeng, Z.-C.; Rao, W.; Zhang, S. Detecting the Responses of CO_2 Column Abundances to Anthropogenic Emissions from Satellite Observations of GOSAT and OCO-2. *Remote Sens.* **2021**, *13*, 3524. https://doi.org/10.3390/rs13173524

Academic Editor: Michael Obland

Received: 25 July 2021
Accepted: 3 September 2021
Published: 5 September 2021

1. Introduction

Global atmospheric CO_2 concentration continues to increase by 2–3 ppm per year, which contributes significantly to global warming [1,2]. Changes in atmospheric CO_2 concentrations are primarily driven by emissions from human activities, photosynthesis of natural terrestrial ecosystems, and biogeochemical processes in the ocean. To achieve the goal of curbing global warming proposed by the Paris Agreement in 2015, many countries put forward the strategy of carbon neutrality. They are committed to limit global average temperature rise to be below 1.5° above pre-industrial levels through different effective ways of reducing greenhouse gas emissions [3,4]. To achieve these goals, it is critical to investigate the spatio-temporal changes of atmospheric CO_2 concentration and detect the influence mechanism of human activities in various regions on atmospheric CO_2 variations, so as to provide a basis for governments to evaluate the effects of CO_2 emission reduction measures.

Satellite measurements from GOSAT and OCO-2 have delivered the column-averaged dry air mole fractions of CO_2 (XCO_2) data for more than 12 years, which provide data for studying long-time variations of global and regional carbon emissions [5–11]. It has become an effective data source for understanding the contributions of natural ecosystems and human activities to the increase of atmospheric CO_2 concentration. For example, using satellite XCO_2 observations from GOSAT and OCO-2, many studies have found that extreme climate related to the El Niño Southern Oscillation (ENSO) disturbs the interannual increase of atmospheric CO_2 concentration at global and regional scales [12–16]. Abnormal increase in CO_2 concentration mostly occurs in natural vegetation areas. The detection and attribution analysis of extreme CO_2 changes show that CO_2 anomalies are related to the abnormal carbon emissions from terrestrial ecosystems caused by extreme climate [17]. Previous studies using CO_2 data from model and ground observations also showed consistent results with that from satellite observations [18–22].

XCO_2 enhancements could be detected by satellite observations in large cities, power plants, volcanoes, and fire emissions. By differencing the observations over a megacity with those in the nearby background, XCO_2 enhancements can be derived. The enhancement is found to be more than 3 ppm in large cities, such as Beijing-Tianjin-Hebei areas and the Yangtze River Delta in China, the Los Angeles megacity in the USA, the Seoul Metropolitan area in South Korea, and Mumbai in India [23–29]. XCO_2 observations from OCO-2 have also been used to identify enhanced plume signals and estimate anthropogenic emissions from individual point sources such as power plants and volcanoes [30–32]. For Australian mega bushfires, fire-induced XCO_2 enhancement detected by three orbits of observations from OCO-2 during November–December in eastern Australia is approximately 1.5 ppm [33]. Global XCO_2 anomalies derived from satellite observations agree well with the spatial patterns of emission inventories and model simulations [34–36]. Furthermore, an assessment combining satellite XCO_2 observations and other relatively short-lived pollutants (e.g., CO and NO_2) in cities found that urban CO_2 enhancements have a good correlation with air pollutants, which can be used to evaluate emission characteristics, such as combustion efficiency [36–38]. These results indicate that satellite XCO_2 observations have the detectability of natural and anthropogenic CO_2 emissions. Combined with ground-based measurements, they provide reliable data sources for constraining anthropogenic emission estimates and verifying bottom-up inventories.

However, previous studies on the detectivity of using satellite XCO_2 observations for anthropogenic emissions still have some limitations. Due to the impact of data sparsity in space and time caused by impacts from geophysical factors such as aerosols and clouds, most existing studies focus on individual areas or specific events, but lack sufficient analysis at global and regional scales. In response to this problem, we generated a dataset of global land mapping XCO_2 data (Mapping-XCO_2) using GOSAT and OCO-2 observations. With these global spatio-temporal continuous XCO_2 data, this study is able to fully explore the changes of XCO_2 enhancements caused by anthropogenic emission at both global and regional scales.

In this paper, we investigate global XCO_2 variations in space and time, and analyze spatial patterns of seasonal XCO_2 changes affected by atmospheric transport and terrestrial biosphere. We further focus on urban agglomerations with high anthropogenic emissions and quantify the responses of regional XCO_2 to anthropogenic emissions. Our study aims to provide global spatial and temporal analysis of XCO_2 changes and quantify the responses of regional XCO_2 enhancements to anthropogenic emission using long-term mapping data generated from satellite XCO_2 observations.

2. Materials and Methods

2.1. Materials

2.1.1. CO_2 Datasets

We use the global land mapping XCO_2 dataset (Mapping-XCO_2) from April 2009 to December 2020, which has a spatial grid resolution of 1° latitude by 1° longitude and temporal resolution of 3 days. The dataset is produced by applying a spatio-temporal geostatistical method to satellite XCO_2 retrievals from GOSAT observations (from April 2009 to August 2014) and OCO-2 observations (from September 2014 to December 2020). The XCO_2 retrievals are the latest ACOS level 2 Lite data product (v9r) and the latest level 2 lite data product (v10r) for OCO-2 [7,10,11]. These products are both obtained from the Goddard Earth Science Data Information and Services Center (GES DISC) [39]. The workflow chart of mapping gridded XCO_2 data are illustrated in Figure A1, including the following key steps: (1) We adjusted the differences in XCO_2 retrievals induced by the *a priori* CO_2 profile and different overpass time using CO_2 profiles from CarbonTracker as reference data. Spatial and temporal scales of satellite observations are integrated to a uniform unit by averaging XCO_2 within 10.5 km and 3 days. (2) The global land is divided into different continental regions and processed separately. In each mapping region, the spatio-temporal correlation structures of the integrated XCO_2 data are assumed to be homogeneous and locally stationary. The spatio-temporal empirical variogram in each region was calculated after removing the spatial and temporal trend from the integrated XCO_2. (3) Based on these variogram models, space-time kriging with moving cylinder kriging neighborhood was implemented to estimate the XCO_2 value at the center of 1° grids. A detailed description of the gap-filling method is referred to Zeng et al. [40–43] and He et al. [43]. We calculated estimation uncertainty for each grid according to the method described in Zeng et al. [42], which shows that the estimation uncertainty of Mapping-XCO_2 is less than 1.5 ppm on average. Compared to TCCON data, the overall bias of Mapping-XCO_2 obtained by $\pm 0.5°$ box centered at the TCCON sites is 0.16 ± 1.19 ppm.

Table 1 gives a summary of Mapping-XCO_2 and the comparisons with model simulations by CarbonTracker and ground-based observations from the World Data Centre for Greenhouse Gases (WDCGG). CarbonTracker simulates global atmospheric CO_2 mole fractions from a combination of CO_2 surface exchange models and an atmospheric transport model driven by meteorological fields [44]. We collected CO_2 data at the local time of 13:30 from CT2019B for comparison analysis with spatio-temporal variations of Mapping-XCO_2. The dataset has a resolution of $3° \times 2°$ grid in space and 1 day in time. In order to analyze long-term trends derived from Mapping-XCO_2, we collected global analysis data of atmospheric CO_2 concentrations and rates of change from WDCGG. The data are produced based on ground observations from the WMO Global Atmosphere Watch (GAW) in situ observational network. Globally averaged CO_2 mole fractions and CO_2 trends cover the period of 1984–2019, with the growth rates range from 1985 to 2018. These data are also reported by the annual WMO Greenhouse Gas Bulletin [2].

Table 1. The products of CO_2 data from satellite observation, model, and ground observation.

Dataset	Description	Reference/Data Source
Mapping-XCO_2	Global land mapping XCO_2 dataset produced by applying spatio-temporal geostatistics on GOSAT and OCO-2 observations from April 2009 to September 2020. The dataset is regularly distributed with a temporal interval of 3 days and spatial interval of 1° grid.	GES DISC [39] Zeng et al. [40–43]
CT-XCO_2	The model XCO_2 data at the local time 13:30 (LST) from CT 2019B from 2009 to March 2019 in 3° × 2° grids with a temporal interval of 1 day.	NOAA [45]
WDCGG-CO_2	Global CO_2 analysis based on ground-based observations, covering from 1984 to 2019 for global monthly mean concentrations and trends and from 1985 to 2018 for growth rates.	WDCGG [46]

2.1.2. Auxiliary Datasets

To analyze the mechanism of XCO_2 changes and its response to anthropogenic emissions, we collected various auxiliary datasets to compare with XCO_2 variations at global and regional scales.

The Open-source Data Inventory for Anthropogenic CO_2 (ODIAC) is used to evaluate high emission areas, which can potentially be detected by satellite observed XCO_2 data. ODIAC is a global gridded emission product based on spatial and temporal disaggregation of country scale emissions [47,48]. The latest version of ODIAC emission data product (ODIAC 2020B) provides monthly CO_2 emissions from 2000 to 2019, including two different spatial resolutions of 1° × 1° and 1 km × 1 km. CO_2 emission estimates of the product are based on the latest country fossil fuel CO_2 emission estimates made by the new Carbon Dioxide Information Analysis Center (CDIAC) team from 2000 to 2017 and its projection using fuel consumption data reported by the BP Statistical Review of World Energy in 2018 and 2019 [49]. We downloaded ODIAC data from 2009 to 2019 from the Center for Global Environmental Research, National Institute for Environmental Studies (CGER-NIES) [49].

We used two ENSO indices, including the Southern Oscillation Index (SOI) and the Oceanic Niño Index (ONI), to analyze the fluctuating response of the global CO_2 growth rate to ENSO events. The indices are both provided by the Physical Sciences Laboratory at the National Oceanic and Atmospheric Administration (NOAA). The SOI is defined as the normalized pressure difference between Tahiti and Darwin based on the method developed by Ropelewski and Jones [50]. The data are obtained from the Climate Research Unit [51]. The ONI is a three-month running mean of sea surface temperature (SST) anomalies in the El Niño region (5°N–5°S, 120°W–170°W). The data are obtained from the NOAA Climate Prediction Center [52].

In order to evaluate the latitudinal zonal pattern of seasonal XCO_2 changes revealed by the satellite XCO_2 data, we compared it with the spatial patterns of potential temperature, which acts as a dynamical tracer of transport of the air masses [53]. Potential temperature is most frequently used in atmospheric sciences because it is not affected by the physical lifting or sinking associated with flow over obstacles or large-scale atmospheric turbulence [26,27,54]. Lines of constant potential temperature are natural flow pathways that are largely horizontal near the surface, and it is tightly correlated with CO_2 in simulations with zonally uniform surface fluxes [53]. In this paper, we used the potential temperature at 1000 hPa and calculated the averaged contours during the period from 2009 to 2020. The potential temperature data are monthly means produced by the NCEP/NCAR reanalysis. The online website is http://www.esrl.noaa.gov/psd/cgi-bin/data/composites/printpage.pl (accessed on 15 June 2021).

To analyze the influence of the terrestrial ecosystem on the global carbon cycle, we collected the Normalized Difference Vegetation Index (NDVI) data and the land cover type derived from the Moderate Resolution Imaging Spectroradiometer (MODIS) observation. These datasets are downloaded from the website https://ladsweb.modaps.eosdis.nasa.gov/ (accessed on 8 March 2021). NDVI data from the MOD13C2 product have temporal and spatial resolutions of 0.05° and 2 days, respectively [55]. We calculated global monthly mean data with 1° resolution from 2009 to 2020, which are used for correlation analysis with seasonal XCO_2 changes from Mapping-XCO_2. The land cover type is from the MCD12C1 product. We used the land cover type of the International Geosphere Biosphere Programme (IGBP) scheme, which includes 11 natural vegetation classes, 3 developed and mosaicked land classes, and 3 non-vegetated land classes. For regional studies, the land cover type is classified into urban, croplands, vegetation, and other.

NO_2 is a short-lived gas mostly co-emitted from fossil fuel combustion by industries and vehicles. It has been shown to be a good tracer for anthropogenic CO_2 emissions [36–38]. NO_2 data used in our studies is the level 3 offline NO_2 data product derived from TROPOMI/Sentinel-5 Precursor observations [56,57]. The data product provides the total vertical column of NO_2 concentrations with temporal and spatial resolutions of 2 days and 0.01° grid, respectively. The dataset is delivered by the European Space Agency (ESA) and publicly available on Google Earth Engine [57,58]. We obtained regional NO_2 columns in the study areas from July 2018 to December 2020 to assist the analysis of regional emission characteristics.

2.2. Methods

2.2.1. Calculation of Global Temporal XCO_2 Variations Using Mapping-XCO_2

The time series of atmospheric XCO_2 is basically a combination of three signals: a long-term trend, a seasonal cycle, and short-term variations [59]. To extract the temporal characteristics of XCO_2 variations, the most common method is to assume that the long-term trend and seasonal cycles can be represented by a polynomial function and a sum of seasonal harmonics, respectively [17,42,60–62]. As shown in Equation (1), we applied curve fitting to global gridded XCO_2 from Mapping-XCO_2 using a linear least squares regression method:

$$f(t) = a_0 + a_1 t + a_2 t^2 + \sum_{i=1}^{4} (\beta_i \sin(i\omega t) + \gamma_i \cos(i\omega t)) \tag{1}$$

$$XCO_2 = f(t) + \delta, \tag{2}$$

where $f(t)$ is the fitting result, t is the time in a unit of 3 days (122 cycles per year), ω is a parameter of the temporal period in yearly harmonics calculated by 2π/122. The parameters of $a_0, a_1, a_2, \beta_i, \gamma_i$ are obtained by least squares fitting. Note that the residuals (δ) between global mapping XCO_2 data and $f(t)$ in Equation (2) include a part of information on interannual and short-term variations that are not represented by the function. We use a low-pass filter to filter the residuals and obtain the signals of interannual and short-term variations [59,60]. Global monthly XCO_2 and its long-term trend are calculated by combining the fitting part of the function and the filtered part. The growth rate of global XCO_2 is computed by taking the derivative of the long-term trend of XCO_2.

2.2.2. Clustering Spatial Pattern of the Seasonal XCO_2 Cycle

The changes of XCO_2 show a seasonal cycle especially in the Northern Hemisphere, which is affected by CO_2 flux from atmospheric transport and the terrestrial biosphere. The seasonal XCO_2 cycle for each grid is obtained by fitting XCO_2 timeseries of the grid using Equation (1), which also characterizes the long-term trend and a seasonal cycle for each grid. We utilized an unsupervised K-means method to cluster the XCO_2 based on the similarities in its seasonal cycles in order to obtain the spatial pattern of seasonal XCO_2 changes. K-means is an iterative algorithm used to classify the given dataset based on the similarity of temporally changing features where those grids with similar seasonal XCO_2 changes are classified into the same cluster [63]. The temporal variation of XCO_2, after removing long-term trends for each grid, reflects the biospheric fluxes from vegetation seasonal activities coupled with the atmospheric transport. This clustering method groups those grids with similar temporal variations to the same class. The clustering results are able to reveal the spatial patterns of atmospheric transport and terrestrial ecosystems' CO_2 uptake.

2.2.3. Detecting CO_2 Anomalies at Global and Regional Scales

The global atmospheric CO_2 concentration represents a balance of all natural and anthropogenic CO_2 fluxes into and out of the atmosphere. Atmospheric CO_2 is well mixed by turbulent mixing and atmospheric transport [2]. We use global monthly averaged XCO_2 as the global background. Gridded XCO_2 anomalies are calculated as the differences between gridded XCO_2 data and the background, which is hereafter referred to as $dXCO_2$. The $dXCO_2$ is associated with net CO_2 fluxes in the grid. A negative $dXCO_2$ implies a net sink of CO_2, while positive $dXCO_2$ implies a net source relative to global background. The spatial distribution of global gridded $dXCO_2$ from Mapping-XCO_2 is described in Section 3.1 and is further compared with $dXCO_2$ from CT-XCO_2 data.

Lastly, we focus on urban agglomerations in China and the USA to demonstrate regional detectivity of CO_2 anomalies induced by anthropogenic emission. The urban agglomerations with high emissions are selected as study areas, which are basically located in the same latitude zone of 25°–45°. In order to remove large-scale CO_2 variations, median XCO_2 in the latitude zone is utilized as a background value. We computed regional XCO_2 anomalies(ΔXCO_2) by subtracting the "background" from regional averaged XCO_2 in the study areas.

3. Results

3.1. Spatio-Temporal Characteristic of Global XCO_2 Variations and Anthropogenic Emissions

We calculated global gridded anomalies ($dXCO_2$) from Mapping-XCO_2 and CT-XCO_2 to analyze global XCO_2 variations in space and time. Figure 1 shows spatial distributions of multi-year averaged $dXCO_2$ of Mapping-XCO_2 during 2010–2018, which have a similar spatial pattern with that calculated from CT-$dXCO_2$ in Figure A2. Higher positive $dXCO_2$ is observed in the region of East Asia, Southeast Asia, Middle East, North America, and North Africa. The $dXCO_2$ shows a negative value in the Southern Hemisphere. The result from Mapping-XCO_2 is about 0.4 ppm lower than CT-XCO_2 in eastern Asia. However, it shows obvious higher $dXCO_2$ over the regions of Xinjiang in China and lower $dXCO_2$ in India. The overall difference of global monthly mean XCO_2 between Mapping-XCO_2 and CT-XCO_2 is -0.24 ± 0.39 ppm, which is less than the difference of $dXCO_2$. Therefore, the differences of global XCO_2 anomalies between Mapping-XCO_2 and CT-XCO_2 are mostly induced by their gridded XCO_2 data. As can be seen in Figure A3, the large difference is mainly distributed in southern Eurasia. This large difference is very likely caused by sparse satellite observations that lead to higher mapping uncertainty, especially between 2010 and 2014.

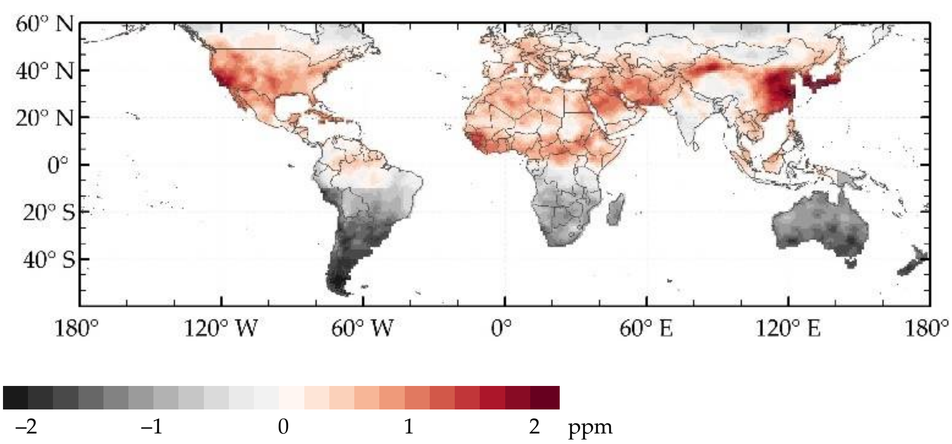

Figure 1. Spatial distributions of the averaged $dXCO_2$ from 2009 to 2018 calculated from Mapping-XCO_2.

Seasonal dXCO_2 in winter and summer are computed by averaging dXCO_2 values during December-January-February (DJF) and June-July-August (JJA), respectively. Figure 2 maps spatial patterns of seasonal dXCO_2 from Mapping-XCO_2 from 2009 to 2020. During wintertime, ecosystem CO_2 uptake tends to be minimal over the Northern Hemisphere so that the dXCO_2 is mostly caused by CO_2 emissions from fossil fuel combustions. Positive dXCO_2 of 1–2 ppm could be clearly observed in eastern China, eastern USA, and Europe in the Northern Hemisphere. The regions from the equator to 15° N have positive dXCO_2 values greater than 1 ppm in winter and lower dXCO_2 about 0.31 ppm in summer, which may be attributed to seasonal biomass burning [23,35,64]. In summer, the regions over the northern high latitudes show the largest negative dXCO_2 because terrestrial ecosystems in the Northern Hemisphere take up CO_2 emitted by human activities. CO_2 anomalies in the Southern Hemisphere are negative in winter and positive in summer, excluding the regions in tropical Africa. These spatial characteristics are generally similar to dXCO_2 calculated by CT-XCO_2 in Figure A4. Positive dXCO_2 in summer from CT-XCO_2 is slightly higher than the result of satellite XCO_2 data. The main difference is that there are no consistent changes of dXCO_2 in tropical Africa between Mapping-XCO_2 and CT-XCO_2, which may be due to the underestimation of fire emissions in CT simulation.

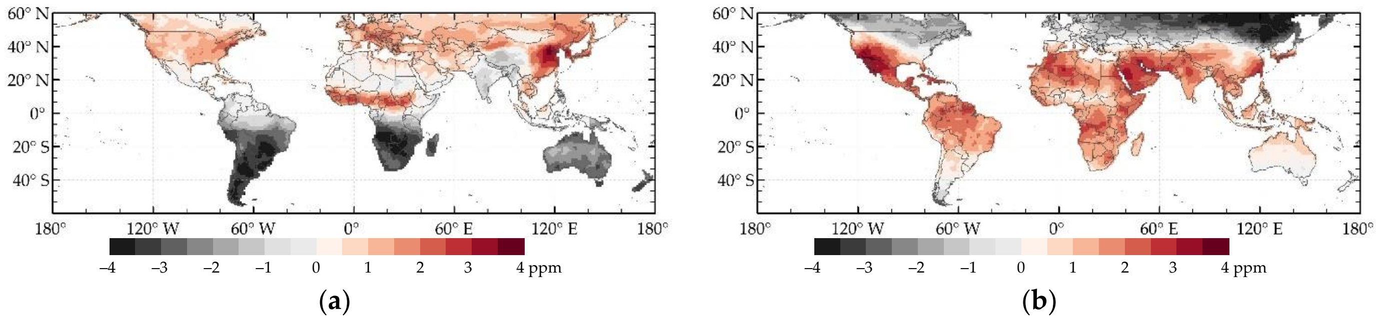

Figure 2. Spatial distributions of seasonal dXCO_2 in winter (**a**) and in summer (**b**) calculated using Mapping-XCO_2 from 2009 to 2020.

Comparing the spatial distribution of anthropogenic emissions from the ODIAC emission inventory in Figure 3, we can see that these regions with positive dXCO_2 of 1–2 ppm are very consistent with high anthropogenic emissions. As shown in Figures 2a and A4a, the pattern of dXCO_2 in the United States during wintertime shows larger dXCO_2 in the east than that in the west, which is similar to the pattern of CO_2 emissions from ODIAC. Additionally, the high CO_2 absorption by natural terrestrial biosphere in the western region during summertime, because of the high emissions as indicated by ODIAC, is not found in the multi-year mean dXCO_2. These results indicate that global CO_2 anomalies in winter can effectively represent the increase in atmospheric CO_2 concentration caused by anthropogenic emissions and biomass burning.

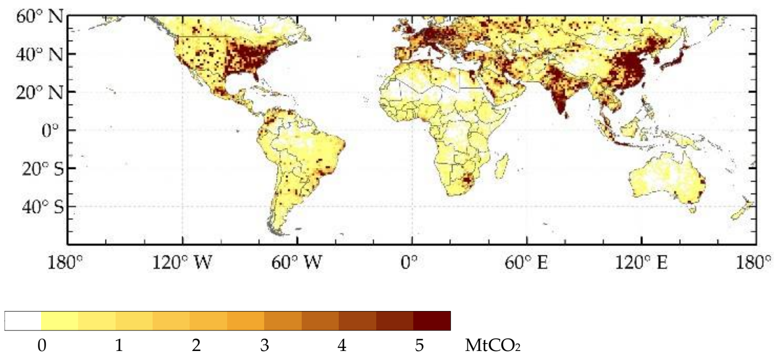

Figure 3. Long-term average of global CO_2 emissions in 1° grid from ODIAC during the period of 2009 to 2019.

Figure 4a shows the global CO_2 growth rates derived from Mapping-XCO_2, CT-XCO_2, and the ground-based CO_2 measurements from WDCGG. Compared with CT-XCO_2, the global CO_2 growth rates calculated by Mapping-XCO_2 are more consistent with observational data. Annual mean CO_2 growth rates of 1.82 to 2.98 ppm are reflected on the continuous increases in atmospheric CO_2 concentration, which is mainly caused by anthropogenic CO_2 emissions. High growth rates appeared in 2010, 2012/2013, and 2015/2016. Among them, the growth rate in 2015/2016 was the highest. Many studies have pointed out that significant inter-annual fluctuations are induced by abnormal natural CO_2 emissions associated with ENSO events [2,16]. For that, we also compared the annual CO_2 growth rate from Mapping-XCO_2 with two ENSO indices, which are shown in Figure 4b. The result shows the satellite-derived growth rates agree well with ENSO indices. The correlation of the annual CO_2 growth rate with SOI and ONI are −0.52 and 0.68, respectively. The growth rate response as quantified by the correlation coefficient (R) is largest after 4 months for SOI (R^2 = 40.24%) and after 3 months for ONI (R^2 = 58.46%). These results are consistent with previous reported findings [16,18,20,22].

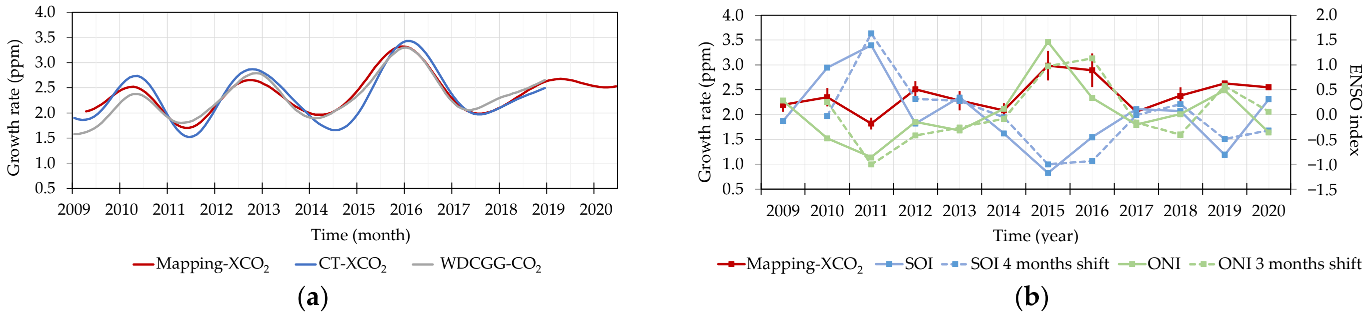

Figure 4. Time series of global CO_2 growth rate from 2009 to 2020 and comparison with ENSO indices. (**a**) Global growth rates of the long-term CO_2 trend from Mapping-XCO_2, CT-XCO_2, and ground-based observations of CO_2 data; (**b**) comparison of satellite-derived growth rate (red line) and ENSO indices. The 1σ uncertainty range of the growth rates are shown as vertical lines. The original ENSO indices are shown as solid lines and time-shifted data are shown as dotted lines.

3.2. Spatial Pattern of the Seasonal XCO_2 Cycle

Global seasonal XCO_2 changes from 2009 to 2020 are grouped into 40 clusters based on the K-means method as described in Section 2.2.2. Figure 5 presents spatial distribution of the clustering results. We noted that seasonal XCO_2 changes show latitudinal zonal distribution but significantly offset to the southwest in the Northern Hemisphere. These interesting results are highly consistent with the pattern of clusters derived from CT-XCO_2 using the same approach in Figure A5. Compared to the distribution of potential temperature in Figure 6, the spatial pattern of seasonal XCO_2 changes is in good agreement with potential temperature contours, especially in the Northern Hemisphere. The result indicates that clustered XCO_2 variation is relatively homogeneous, which allows us to detect any perturbations due to the external CO_2 fluxes within each cluster region. Moreover, seasonal amplitudes of XCO_2 gradually reduce from north to south as shown in Figure 5b. The maximum is up to 10 ppm in cluster 1, and the minimum is 5 ppm in cluster 5, which is primarily caused by the strength of vegetation uptake at different latitudes.

We further investigated the relationship between seasonal XCO_2 changes and seasonal vegetation activities characterized by NDVI. Figure 7 shows the spatial distribution of correlation coefficients (R) between their seasonal changes globally. The seasonal XCO_2 presents strong negative correlation with NDVI in most areas due to seasonal activities of vegetation CO_2 uptake in the northern high latitude area and regions of grassland and savannas. The regions with less or no vegetation present weak correlation between seasonal XCO_2 and NDVI. These regions with strong correlations indicate that the biosphere has large impacts on the variation of CO_2 concentration, which can also be seen in Figure A6.

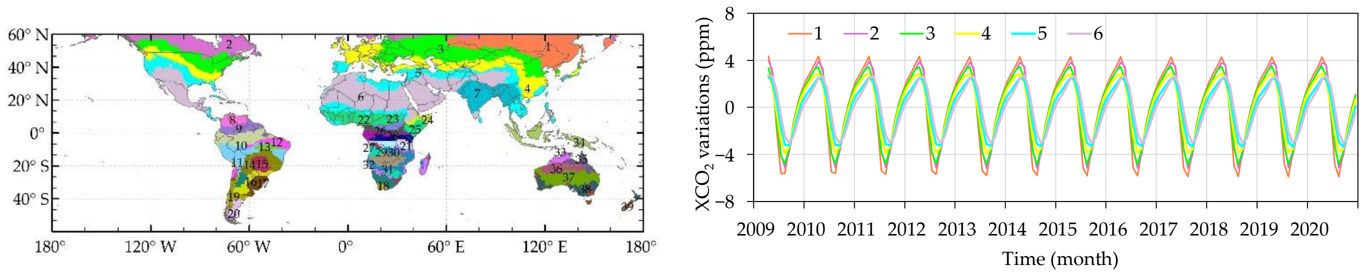

(**a**) (**b**)

Figure 5. The clustering results of seasonal XCO_2 changes based on Mapping-XCO_2 from 2009 to 2020 (**a**) and the temporal variations of clusters in the Northern Hemisphere (**b**). The line colors correspond to the clusters in (**a**).

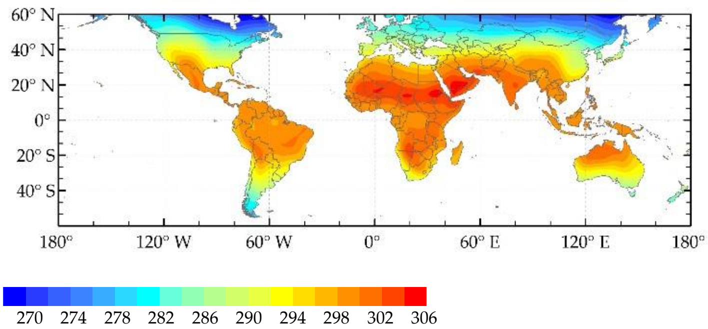

Figure 6. Spatial distribution of potential temperature contours at 1000 hPa from 2009 to 2020.

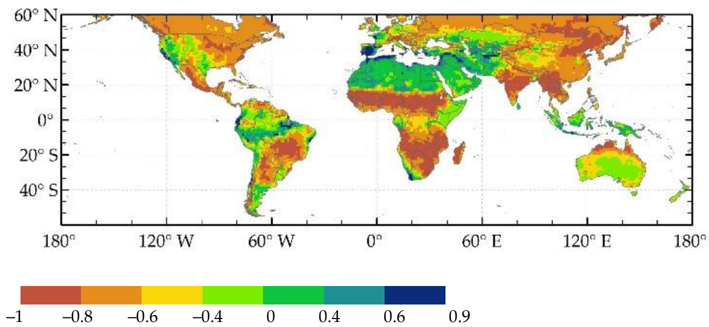

Figure 7. Spatial distribution of correlation coefficients between seasonal XCO_2 changes based on Mapping-XCO_2 and NDVI from 2009 to 2020.

An accurate assessment of the contribution of the biosphere and atmospheric transport helps better disentangle the contribution of anthropogenic emissions to XCO_2 variations. This clustering result can help us understand globally spatial distribution characteristics of XCO_2 variation affected by the biosphere and atmospheric transport. Comparing Figure 5a with Figures 6 and 7, we can find that clustering results of XCO_2 after removing long-term changes effectively reveal the effects of fluxes from the biosphere and atmospheric transport. The ranges of clustering classes can be used to select and analyze interesting areas with similar biospheric fluxes and atmospheric transport.

3.3. Regional XCO_2 Anomalies and Anthropogenic Emissions

3.3.1. Regional XCO_2 Anomalies in Urban Agglomeration Areas

We focus on the investigation of regional XCO_2 anomalies caused by anthropo-genic emissions in the urban agglomeration areas in China and the United States. Based on the density of cities, we selected three source areas of anthropogenic emissions (AE), including the Beijing-Tian-Hebei region and nearby areas (BTH), the Yangtze River Delta urban agglomerations (YRD), and the urban agglomerations in the eastern United States of America (EUSA), which are shown in Figure 8. Total CO_2 emissions from these areas account for about 13% of global CO_2 emissions according to anthropogenic emissions from ODIAC. These three regions are located in the same clustering areas that have similar seasonal XCO_2 cycles. They are clusters 3 and 4, as shown in Figure 5.

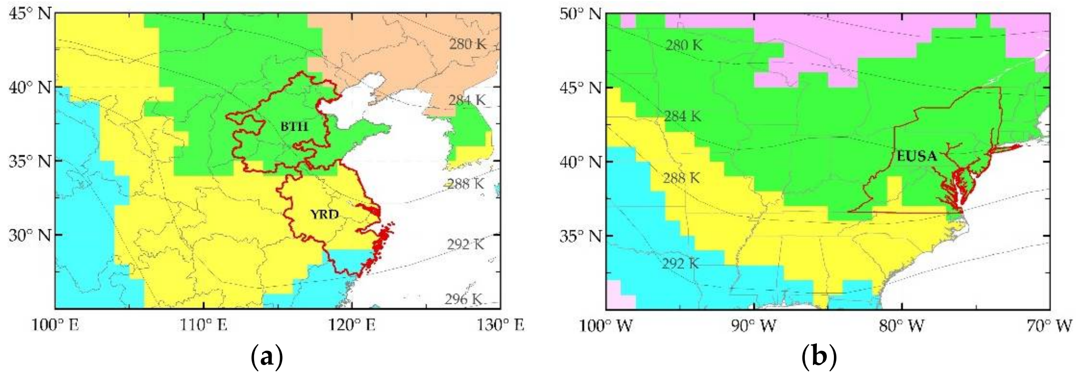

Figure 8. Location of source areas in China and the USA. (**a**) The areas for BTH and YRD; (**b**) the area for EUSA. The red boundary represents source areas. The clustering results from Figure 5 and the lines of potential temperature are also indicated.

Regional XCO_2 anomalies (ΔXCO_2) are calculated by removing the "background" trend of latitude zone from regional CO_2 concentrations as described in Section 3.1. We calculated the multi-year averaged ΔXCO_2 for these three regions using Mapping-XCO_2 according to two stages during 2009–2014 and during 2015–2020, respectively. From Table 2, ΔXCO_2 are generally 1–3 ppm and the values during the wintertime are up to 1 ppm larger than the multi-year mean, especially for BTH and EUSA. Both BTH and EUSA are basically located in cluster 3 with a seasonal amplitude of 8 ppm, which is larger than the amplitude of 6 ppm for YRD in cluster 4. From the first 5 years of 2009–2014 to the second 5 years of 2015–2020, ΔXCO_2 increased in the three areas. Comparing the differences of ΔXCO_2 among AE areas, ΔXCO_2 in both BTH and YRD is greater than that in EUSA, while BTH is slightly larger than YRD.

Table 2. Regional characteristics in the emission source areas.

Source Areas	2009–2014			2015–2020		
	BTH	**YRD**	**EUSA**	**BTH**	**YRD**	**EUSA**
XCO_2 (ppm)	393.96 ± 3.55	394.14 ± 3.44	392.91 ± 3.56	407.56 ± 4.73	407.86 ± 4.87	406.77 ± 4.71
ΔXCO_2 (ppm)	1.24 ± 0.24	1.42 ± 0.31	0.19 ± 0.19	1.36 ± 0.16	1.66 ± 0.22	0.57 ± 0.08
XCO_2 in winter (ppm)	395.29 ± 3.49	395.12 ± 3.33	394.41 ± 3.55	409.40 ± 4.43	409.06 ± 4.56	408.14 ± 4.51
ΔXCO_2 in winter (ppm)	2.32 ± 0.38	2.16 ± 0.34	1.44 ± 0.41	2.59 ± 0.33	2.25 ± 0.37	1.33 ± 0.25
Total CO_2 emission ($GtCO_2$/year)	1.54 ± 0.14	1.66 ± 0.04	0.72 ± 0.01	1.71 ± 0.19	1.86 ± 0.05	0.70 ± 0.01
Land cover (%) (Urban; Croplands; Vegetation; Other)	7.6 34.9 51.2 6.3	7.8 56.4 34.4 1.4	9.7 13.5 74.7 2.2	8.4 34.5 50.6 6.6	8.3 55.4 35.0 1.5	9.7 14.1 73.9 2.3

Time series of XCO_2 anomalies in source areas from Mapping-XCO_2 and CT-XCO_2 are shown in Figures 9 and A7, respectively. ΔXCO_2 shows seasonal variations in which BTH and EUSA present greater negative ΔXCO_2 than YRD. This is likely induced by the vegetation CO_2 uptake as the vegetation coverage is larger in BTH and EUSA. As can be seen from Figure 7, the correlation coefficients between seasonal CO_2 cycles and NDVI are -0.80 ± 0.11 and -0.77 ± 0.05 for BTH and EUSA, respectively, which are greater than the obtained coefficients of -0.65 ± 0.15 for YRD.

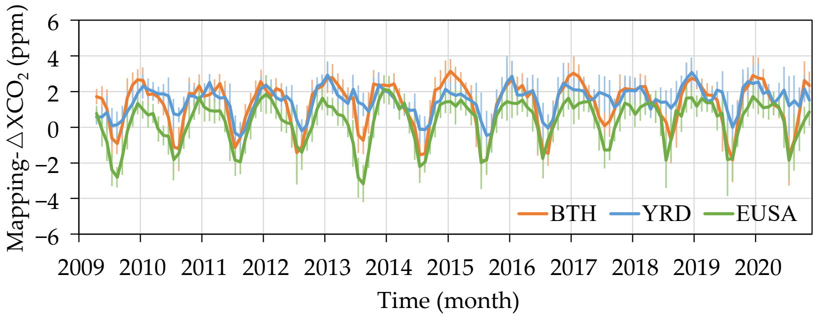

Figure 9. Time series of regional XCO_2 anomalies(ΔXCO_2) in the source areas derived from Mapping-XCO_2. The 1σ uncertainty estimate of regional XCO_2 anomalies is represented by the error bar, which is computed by the averaging mapping uncertainty and the standard deviation of regional statistics.

3.3.2. Response of Regional XCO_2 Anomalies during the COVID-19 Pandemic

Beginning from December 2019, Coronavirus disease 2019 (COVID-19) has occurred in numerous countries. The decline of economic activities caused by the pandemic lockdown measures has led to sharp reductions in anthropogenic CO_2 emissions in many countries. Regional-scale COVID-19-related CO_2 emission reductions are expected to be the largest in the first months of the pandemic outbreak. According to Le Quéré et al. [65], China's CO_2 emissions decreased by 242 $MtCO_2$ (uncertainty range 108–394 $MtCO_2$) during January–April 2020. Buchwitz et al. [66] estimated the relative change of East China monthly emissions in 2020 relative to previous months. Their results showed significant differences across the ensemble of GOSAT and OCO-2 data products analysis. The ensemble mean indicates emission reductions by approximately 8% ± 10% in March 2020 and 10% ± 10% in April 2020 (uncertainties are 1-sigma), while somewhat lower reductions for the other months in 2020. These reduction months, however, should be investigated further, since the lockdown was mainly implemented during January–March; hence, the emission reduction should be in the same period.

We compared the relative differences of regional XCO_2 anomalies during January–April between 2020 and 2019. CO_2 anomalies in YRD have a slight decrease of 0.17 ppm during January to February in 2020 relative to the same month of 2019, while there has been no decline in CO_2 anomalies for BTH and EUSA. This is because that CO_2 is a long-lived gas, and therefore, it has a high background concentration in the atmosphere. The increase of CO_2 concentration caused by anthropogenic emissions and the decline induced by emission reduction are small variables. The precision of satellite observations and mapping uncertainty makes it difficult to detect weak signals due to the emission reduction.

NO_2 concentration in the atmosphere has been used to infer CO_2 reductions and estimate China's CO_2 emissions during the COVID-19 pandemic [67]. Figure 10 illustrates the time series of regional NO_2 columns from July 2018 to December 2020 and the difference of 2020 relative to the previous year of 2019 for three areas. From Figure 10b, we can find that the sharp declines of NO_2 columns started in January and basically ended in April; NO_2 columns were reduced by 45–51%, 59%–61%, and 30% during January–March for BTH, YRD, and EUSA, respectively. The obvious reduction during the lockdown indicates that NO_2 columns are more sensitive to the reduction of anthropogenic emissions. The reduction, moreover, is lower in BTH than in YRD. This likely implies that the effects of reduced emissions from the decreased traffic volume were due to lockdown measures in YRD. However, there was increased demand for winter heating in BTH, as more people in 2020 had to stay in Beijing during the lockdown compared to former years. Additionally, the BTH area suffered a heavy pollution process from 11–13 February during the lockdown period [68].

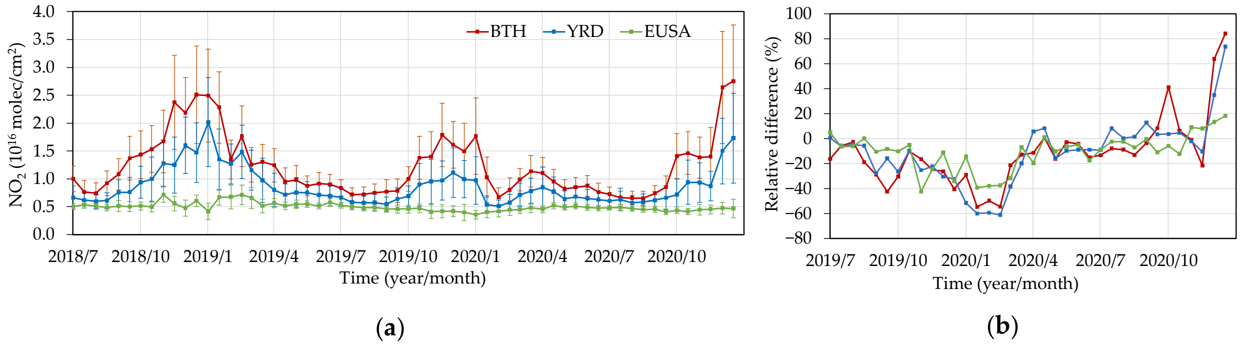

Figure 10. Time series of NO_2 columns and the differences of NO_2 relative to the previous year. (**a**) Regional NO_2 columns every 16 days and 1σ uncertainty estimate is represented by error bar; (**b**) contemporaneous differences of NO_2 between 2019 and 2020.

In order to further analyze the response of XCO_2 to emission reduction in BTH and YRD, we focused on the period from January to March and compared the differences between 2019 and 2020 for ΔXCO_2 and NO_2 columns. ΔXCO_2 was resampled to a 0.01° grid by cubic convolution, which improves spatial resolution without changing the characteristics of the original data. As shown in Figure 11, the differences of ΔXCO_2 between 2020 and 2019 tend to be negative in YRD, which means that emissions reduced, while they tended to increase by approximately 0.5 to 1 ppm in BTH. The spatial pattern of differences for ΔXCO_2 is generally similar to NO_2 columns. The decrease of NO_2 columns in BTH is less than that in YRD. The NO_2 concentration decreased by approximately 35 ± 5% in BTH, while it decreased by approximately 45 ± 8% in YRD.

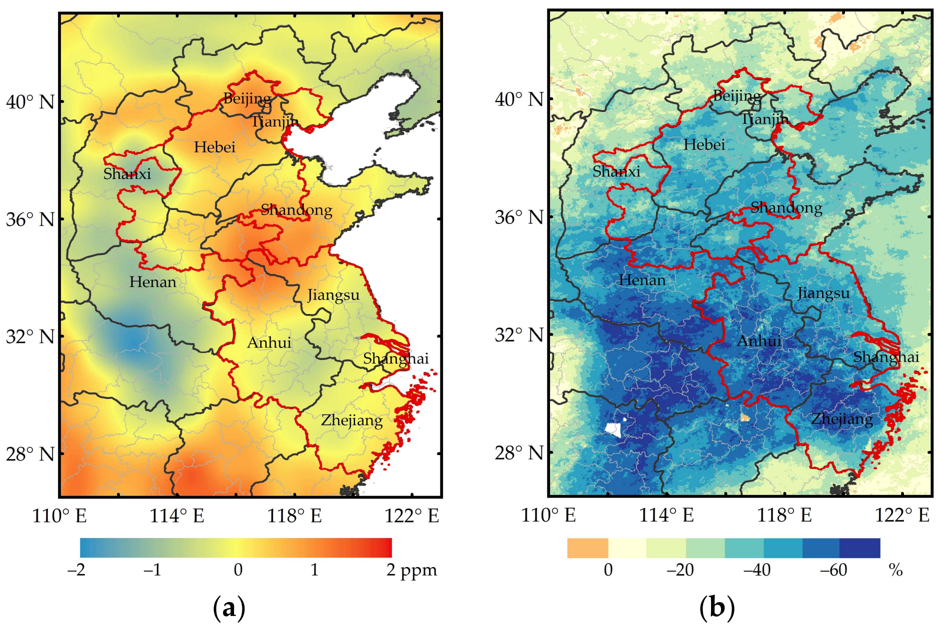

Figure 11. Spatial distribution of changes in XCO_2 anomalies and NO_2 columns from January to March in 2020 and 2019. (**a**) The variations of XCO_2 anomalies and (**b**) the variations of NO_2 columns. The bold gray lines represent the boundary of the provinces, while thin gray lines represent the boundary of cities.

In addition, we computed the variations of ΔXCO_2 and NO_2 columns using the city district as a spatial unit. Figure 12 shows the result where the cities in AE areas are grouped according to provinces. The relationship between ΔXCO_2 and NO_2 shows two distinct features in both BTH and YRD, Shanxi and other provinces in BTH, and Anhui and the other provinces in YRD. These features are likely related to the types of emitting sources in these areas. The emitting sources in Shanxi and Anhui are mostly coal power plants and chemical plants, while the emitting sources of other provinces are mostly gas power plants and vehicles in the megacities of Beijing and Tianjin in BTH and Shanghai, Nanjing, Hangzhou, etc. in YRD. In Shanxi, the reduction of ΔXCO_2 is from -0.3 to -0.9 ppm and the decline of NO_2 is 35% to 42%. In BTH, the reduction of ΔXCO_2 is approximately 0.3 to 0.9 ppm and the decline of NO_2 is 30% to 45%. In comparison, in YRD, there is a larger range of ΔXCO_2 changes, from approximately -0.6 to 1 ppm with declines of NO_2 by 50% to 66% in Anhui. However, for other provinces in YRD other than Anhui, there are smaller changes of ΔXCO_2 from approximately -0.5 to 0.3 ppm, with a decline of NO_2 by 30% to 45%. These results indicate that the relationship between XCO_2 and NO_2 is available for the estimation of CO_2 emissions. However, we should also consider the regional features of emitting sources, since their relationship highly depends on the types of emitting sources.

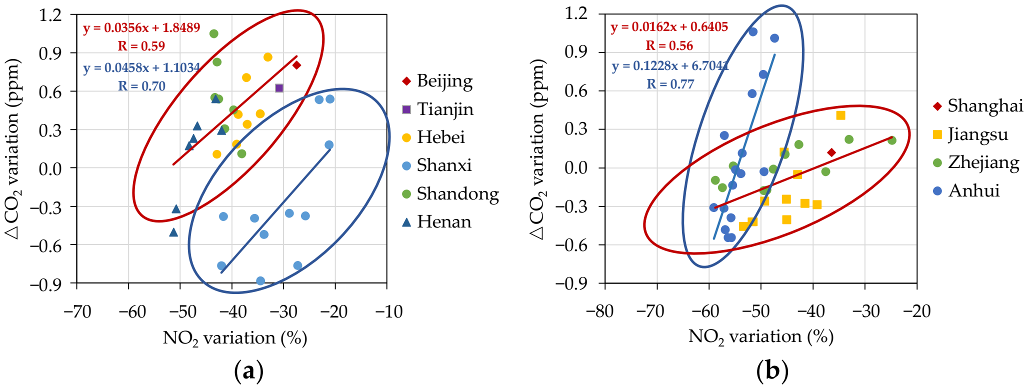

Figure 12. Comparison of NO_2 variations and the changes of XCO_2 anomalies for cities in (**a**) BTH and (**b**) YRD. The variations are relative differences in CO_2 anomalies and NO_2 columns from January to March in 2020 and 2019.

4. Discussion

The accuracy of used Mapping-XCO_2 data will result in uncertainty around the findings of the spatio-temporal feature analysis. As described in Section 2.1.1, Mapping XCO_2 data are obtained by processing different satellite observations using the spatio-temporal geostatistical method. The mapping uncertainty depends not only on the retrieval bias of original XCO_2 retrievals, but also to a large extent on the number of available satellite observations. Mapping uncertainties are calculated by the method of Zeng et al. [43–46]. Figure 13 shows the spatio-temporal distribution of mapping uncertainties. The mapping uncertainties of global grids are generally less than 1.5 ppm. The areas with larger uncertainties are mainly in the high latitude of the Northern Hemisphere, which is due to sparse satellite observations. Mapping uncertainties during the period of GOSAT observations is higher than that corresponds to OCO-2 observations. This is because that the number of GOSAT observations is much less than OCO-2 observations. In the global analysis, CO_2 growth rates derived from Mapping-XCO_2 during 2009 to 2020 are consistent with that from ground-based measures, which does not show the deviation, such as the uncertainty between GOSAT and OCO-2 data. The spatial patterns of mapping gridded XCO_2, in contrast to the global background, are consistent from year to year. These results indicate that the mapping XCO_2 dataset using different satellite observations has consistent distribution characteristics in space and time. Moreover, the relative difference between regional XCO_2 in source areas and the global background is in the range of 1.13 to 3.17 ppm during winter months, which is greater than mapping uncertainty in these areas.

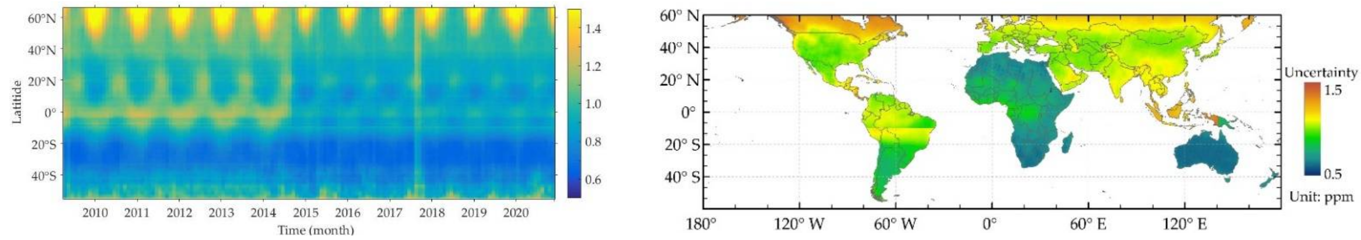

(**a**) (**b**)

Figure 13. Spatio-temporal distribution of mapping uncertainties from Mapping-XCO_2. (**a**) Averaged mapping uncertainty in 1° latitudinal band and 1 month; (**b**) long-term averaged uncertainty from 2010 to 2020.

The land cover types in AE areas are dominated by croplands and vegetation, as shown in Table 2. Affected by the CO_2 uptake of terrestrial ecosystems and the accumulation of CO_2 from anthropogenic CO_2 emissions in the atmosphere, the regional CO_2 concentration reaches the highest value in the spring. The method of CO_2 anomalies can remove large-scale background information from regional CO_2 concentrations and enhance the signal of CO_2 changes. Many studies have pointed out that the calculation method of background concentration does not have a great impact on the results of regional CO_2 anomalies [35]. The temporal characteristic of regional CO_2 anomalies is consistent with that of the regional NO_2 concentration, as shown in Figure 10. Both of them have a maximum during the winter period of each year.

Regional CO_2 anomalies are mainly caused by anthropogenic CO_2 emissions and local ecological CO_2 fluxes. Regional ecological CO_2 flux has little impact on CO_2 changes in winter; CO_2 enhancement is in the range of 1.00 to 3.14 ppm in source areas during winter months, whereas the mapping uncertainty is 0.75 to 1.42 ppm in the same period. During the winter period, ΔXCO_2 of BTH is higher than that of YRD, which agrees with the emission characteristics of NO_2 concentrations. The ΔXCO_2 in BTH and EUSA show negative values in summer, which is because local ecological CO_2 fluxes have a greater impact on CO_2 anomalies in summer. On the other hand, the mapping uncertainty and standard deviation are relatively larger during the summer months. Therefore, it is challenging to detect the enhancement of regional CO_2 concentration caused by anthropogenic emissions in the growing season of vegetation.

5. Conclusions

We presented a global analysis of spatio-temporal XCO_2 variations and detected regional XCO_2 anomalies using satellite mapping XCO_2 data (Mapping-XCO_2) from April 2009 to December 2020. The dataset has resolutions of 3 days in time and 1° grid in space, respectively. Mapping-XCO_2 is produced by a gap-filling technique using XCO_2 retrievals obtained by GOSAT and OCO-2.

The growth rates of global XCO_2 derived from Mapping-XCO_2 data show large fluctuations in inter-annual variabilities, which is in agreement with the long-term CO_2 trends calculated by WDCGG ground-based observations. Elevated XCO_2 of 1.5 to 3.5 ppm, which is mostly induced by anthropogenic emissions and seasonal biomass burning, can be observed using Mapping-XCO_2 data with background removed. Furthermore, the clustering analysis of gridded seasonal XCO_2 variations, after removing the long-term trend and background, reveal spatial pattern of atmospheric transport and terrestrial ecological CO_2 flux.

At the regional scale, XCO_2 enhancements during winter months are detected to be 2.47 ± 0.37 ppm, 2.20 ± 0.36 ppm, and 1.38 ± 0.33 ppm for the Beijing-Tianjin-Hebei area, the Yangtze River Delta area, and the high-density urban areas in the eastern USA, respectively. The regional emission characteristic of XCO_2 enhancement is consistent with regional NO_2 columns. However, it is difficult to accurately detect enhanced CO_2 signals in the vegetation growing season due to impacts of local ecological CO_2 uptakes and relatively large uncertainty of the mapping data during summertime. The regional XCO_2 anomalies did not clearly show the declines of anthropogenic CO_2 emissions during the lockdown of the COVID-19 pandemic from January to March 2020 compared with the same time in the previous year of 2019. However, the significant correlation between relative differences of XCO_2 and NO_2 columns calculated at urban scales indicates that different types of emitting sources show a significantly positive correlation. This result suggests that we could use space-observed NO_2 data to identify the anthropogenic emitting sources and rectify CO_2 emissions estimated from satellite observations since both gases are mostly co-emitted in cities.

Our studies provide new cases for investigating the responses of XCO_2 observed by satellites to anthropogenic emissions at global and regional scales. These results demonstrate the potential of the global land mapping XCO_2 dataset in monitoring the long-term XCO_2 variations and detecting regional XCO_2 enhancements caused by anthropogenic in non-growing seasons.

Author Contributions: Conceptualization, M.S., Z.-C.Z. and L.L.; Data curation, M.S. and S.Z.; Formal analysis, M.S., Z.-C.Z. and L.L.; Methodology, M.S. and L.L.; Software, M.S. and W.R. All authors have read and agreed to the published version of the manuscript.

Funding: This research was funded by the National Key Research and Development Program of China (Grant No. 2020YFA0607503), the Key Program of the Chinese Academy of Sciences (Grant No. ZDRW-ZS-2019-1), and the Strategic Priority Research Program of the Chinese Academy of Sciences (Grant No. XDA19080303).

Acknowledgments: We are grateful for the ACOS-GOSAT v9r data and OCO-2 v10r data, which were provided by the ACOS/OCO-2 project at the Jet Propulsion Laboratory, California Institute of Technology and obtained from the ACOS/OCO-2 data archive maintained at the NASA Goddard Earth Science Data and Information Services Center. CarbonTracker CT2019B results were provided by NOAA ESRL, Boulder, Colorado, USA from the website at http://carbontracker.noaa.gov (assessed on 13 May 2021). We thank NOAA ESRL and PSL for providing potential temperature data and ENSO indices. We thank the European Space Agency (ESA) and Google Earth Engine for providing Sentinel-S5P NO_2 products, CGER-NIES for providing ODIAC data at https://db.cger.nies.go.jp/dataset/ODIAC/ assessed on 29 November 2020 (Data DOI: doi:10.17595/20170411.001), and the World Data Centre for Greenhouse Gases (WDCGG) for providing global atmospheric CO_2 data. We also acknowledge the Land Processes Distributed Active Archive Center (LP DAAC) at the National Aeronautics and Space Administration (NASA) for sharing land cover type and NDVI data derived from MODIS.

Conflicts of Interest: The authors declare no conflict of interest.

Appendix A

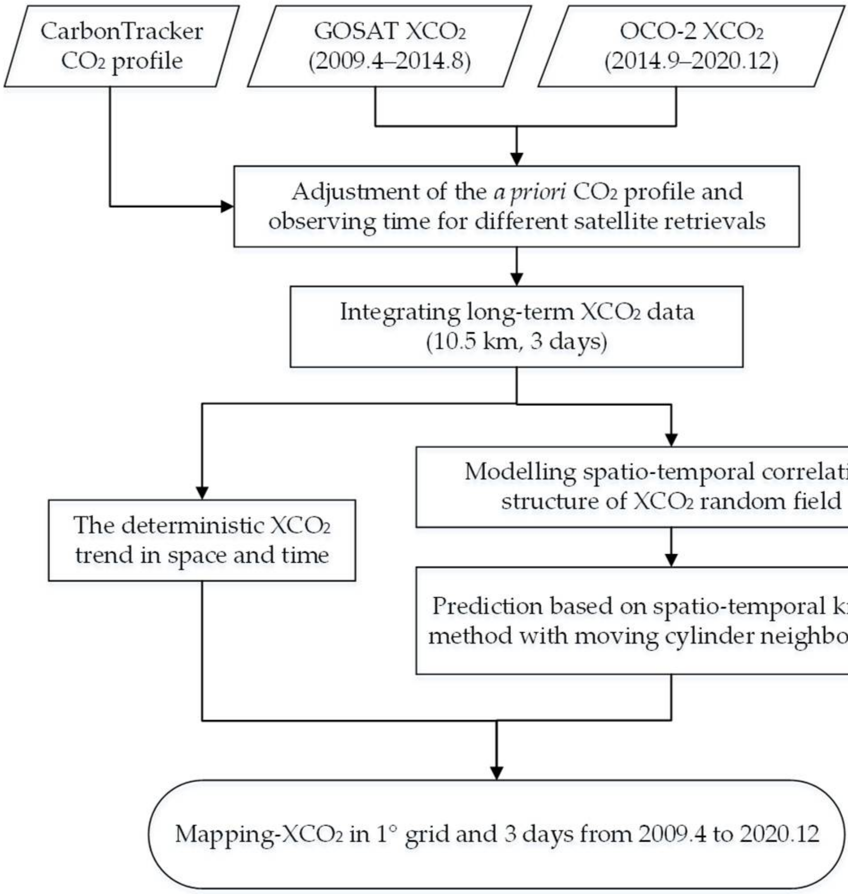

Figure A1. The workflow chart for generating Mapping-XCO_2 using satellite XCO_2 retrievals.

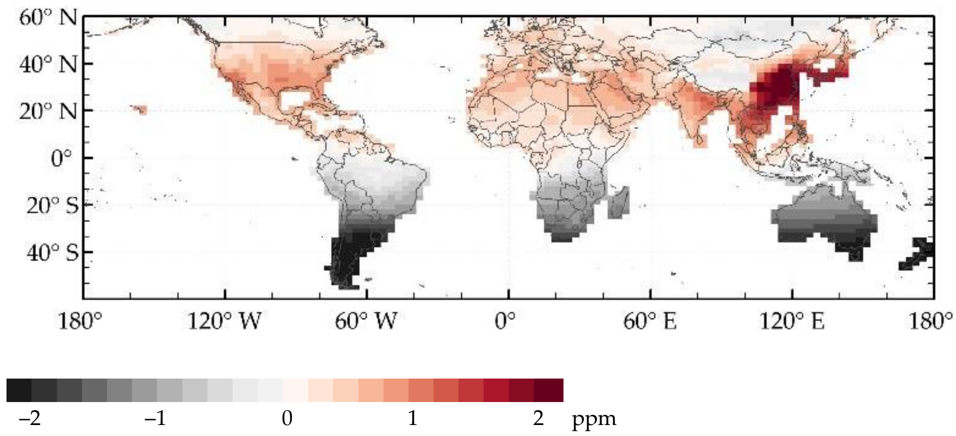

Figure A2. Spatial distributions of averaged $dXCO_2$ from 2009 to 2018 calculated from CT-XCO_2 following the same approach adopted by the Mapping-XCO_2 dataset.

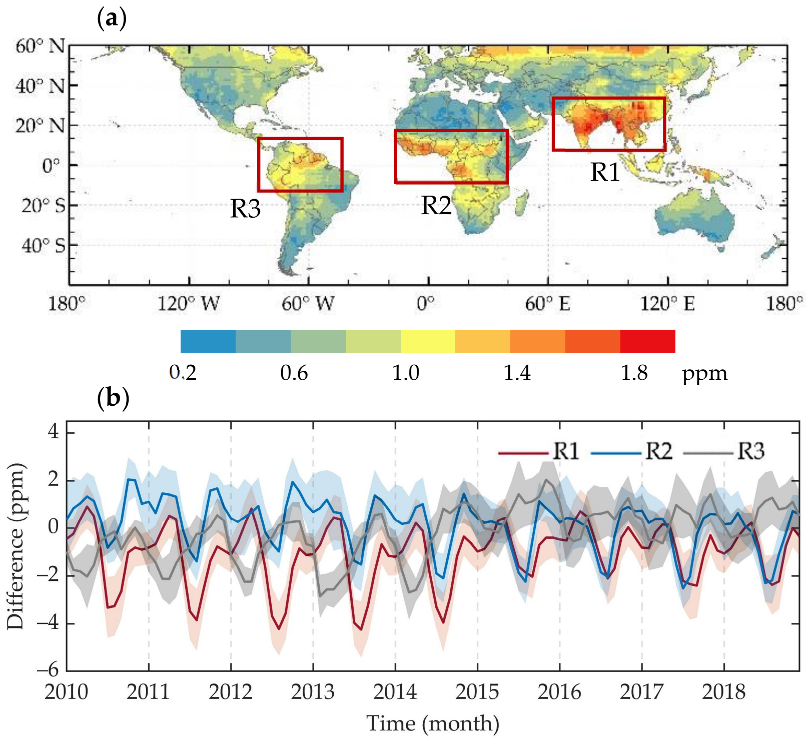

Figure A3. Comparison of Mapping-XCO_2 and CT-XCO_2 from 2010 to 2018. (**a**) The absolute mean difference of monthly gridded XCO_2 between Mapping-XCO_2 and CT-XCO_2 from 2010 to 2018; (**b**) time series of the mean difference in the regions of the red boxes shown in (**a**), in which the shaded colors represent one standard deviation.

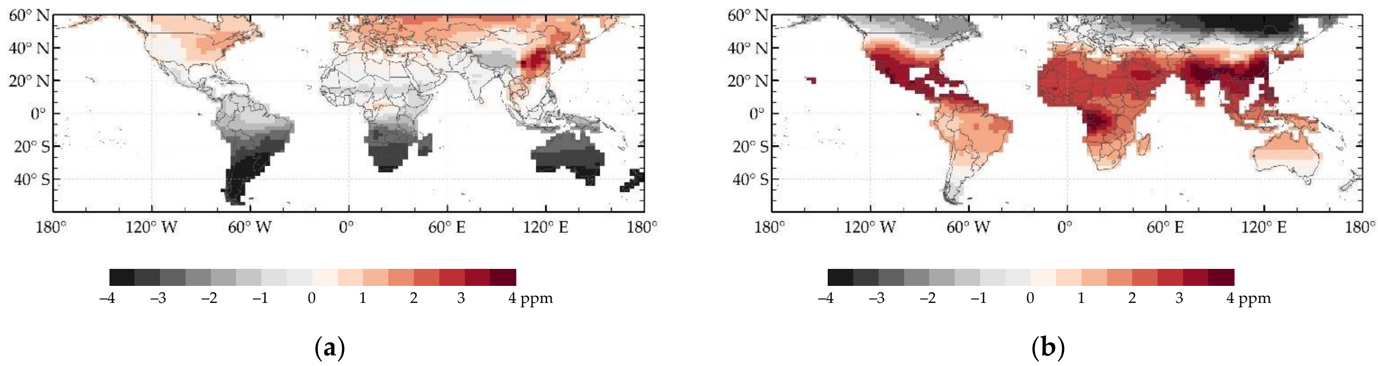

Figure A4. Spatial distributions of long-term averaged seasonal $dXCO_2$ in winter (**a**) and in summer (**b**) calculated from CT-XCO_2 from 2009 to 2018.

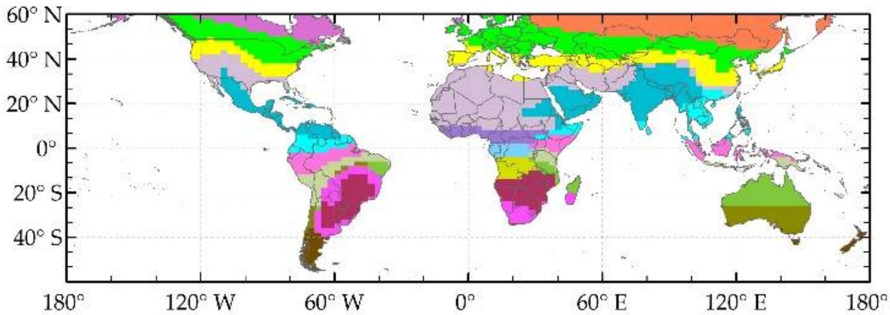

Figure A5. The clustering results of seasonal XCO_2 changes using CT-XCO_2 data from 2009 to 2019.

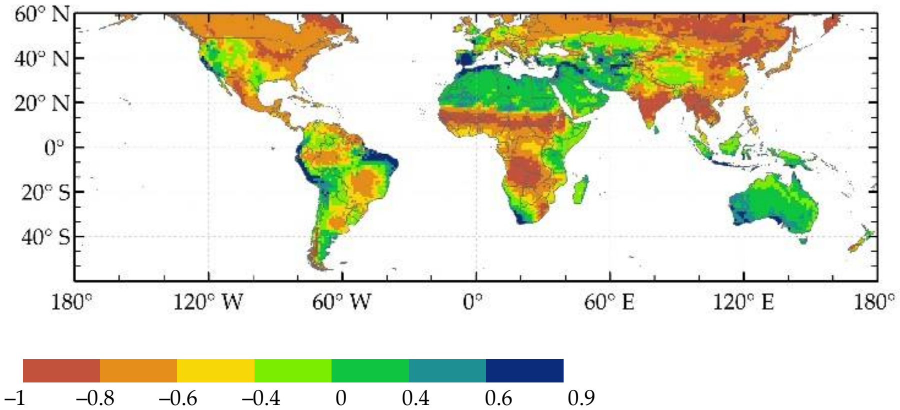

Figure A6. Spatial distribution of correlation coefficients in seasonal XCO_2 changes between CT-XCO_2 and NDVI from 2009 to 2019.

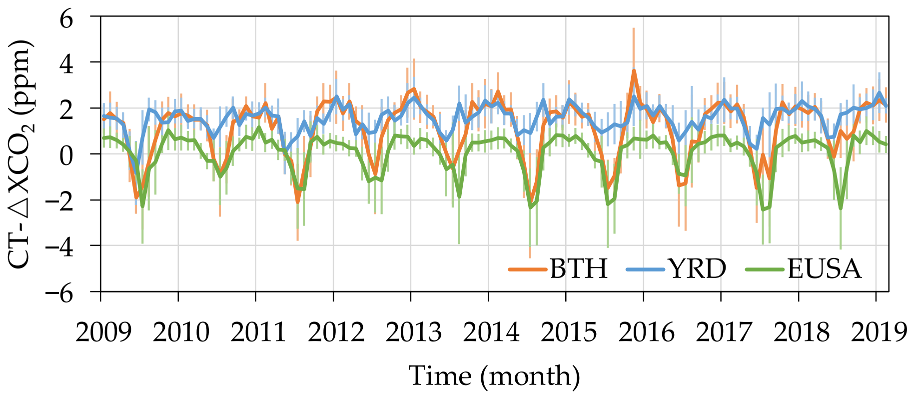

Figure A7. Time series of regional CO_2 anomalies(ΔXCO_2) in the source areas derived from CT-XCO_2. The 1σ uncertainty estimate of regional XCO_2 anomalies is represented by error bar, which is one standard deviation of the regional statistics.

References

1. Friedlingstein, P.; O'Sullivan, M.; Jones, M.W.; Andrew, R.M.; Hauck, J.; Olsen, A.; Peters, G.P.; Peters, W.; Pongratz, J.; Sitch, S.; et al. Global Carbon Budget 2020. *Earth Syst. Sci. Data* **2020**, *12*, 3269–3340. [CrossRef]
2. World Meteorological Organization. WMO Greenhouse Gas Bulletin No. 16. 2020. Available online: https://www.eenews.net/assets/2020/11/23/document_ew_05.pdf (accessed on 2 March 2021).
3. Coulter, L.; Canadell, J.; Dhakal, S. Global Carbon Project Report No. 6, Earth System Science Partnership Report No. 5, Canberra. Global Carbon Project (2008) Carbon Reductions and Offsets. Available online: https://www.globalcarbonproject.org/carbonneutral/index.htm (accessed on 22 February 2021).
4. Defining Carbon Neutrality for Cities & Managing Residual Emissions. Available online: https://www.c40.org/researches/defining-carbon-neutrality-for-cities-managing-residual-emissions (accessed on 31 January 2021).
5. GOSAT Project. Available online: www.gosat.nies.go.jp (accessed on 1 June 2020).
6. Orbiting Carbon Observatory. Available online: https://ocov2.jpl.nasa.gov (accessed on 1 June 2020).
7. Crisp, D.; Frankenberg, C.; Messerschmidt, J.; Wennberg, P.O.; Wunch, D.; Yung, Y.L. The ACOS CO_2 retrieval algorithm—Part II: Global XCO_2 data characterization. *Atmos. Meas. Tech.* **2012**, *5*, 687–707. [CrossRef]
8. Nakajima, M.; Kuze, A.; Suto, H. The current status of GOSAT and the concept of GOSAT-2. *Proc. SPIE* **2012**, *8533*, 853306. [CrossRef]
9. Kataoka, F.; Crisp, D.; Taylor, T.E.; O'Dell, C.W.; Kuze, A.; Shiomi, K.; Suto, H.; Bruegge, C.; Schwandner, F.M.; Rosenberg, R. The cross-calibration of spectral radiances and cross-validation of CO_2 estimates from GOSAT and OCO-2. *Remote Sens.* **2017**, *9*, 1158. [CrossRef]
10. O'Dell, C.W.; Eldering, A.; Wennberg, P.O.; Crisp, D.; Gunson, M.R.; Fisher, B.; Frankenberg, C.; Velazco, A. Improved retrievals of carbon dioxide from Orbiting Carbon observatory-2 with the version 8 ACOS algorithm. *Atmos. Meas. Tech.* **2018**, *11*, 6539–6576. [CrossRef]
11. Kiel, M.; O'Dell, C.W.; Fisher, B.; Eldering, A.; Nassar, R.; MacDonald, C.G.; Wennberg, P.O. How bias correction goes wrong: Measurement of XCO_2 affected by erroneous surface pressure estimates. *Atmos. Meas. Tech.* **2019**, *12*, 2241–2259. [CrossRef]

12. Guerlet, S.; Basu, S.; Butz, A.; Krol, M.; Hahne, P.; Houweling, S.; Hasekamp, O.P.; Aben, I. Reduced carbon uptake during the 2010 Northern Hemisphere summer from GOSAT. *Geophys. Res. Lett.* **2013**, *40*, 2378–2383. [CrossRef]
13. Basu, S.; Krol, M.; Butz, A.; Clerbaux, C.; Sawa, Y.; Machida, T.; Matsueda, H.; Frankenberg, C.; Hasekamp, O.P.; Aben, I. The seasonal variation of the CO_2 flux over Tropical Asia estimated from GOSAT, CONTRAIL, and IASI. *Geophys. Res. Lett.* **2014**, *41*, 1809–1815. [CrossRef]
14. Detmers, R.G.; Hasekamp, O.; Aben, I.; Houweling, S.; van Leeuwen, T.T.; Butz, A.; Landgraf, J.; Köhler, P.; Guanter, L.; Poulter, B. Anomalous carbon uptake in Australia as seen by GOSAT. *Geophys. Res. Lett.* **2015**, *42*, 8177–8184. [CrossRef]
15. Heymann, J.; Reuter, M.; Buchwitz, M.; Schneising, O.; Bovensmann, H.; Burrows, J.P.; Massart, S.; Kaiser, J.W.; Crisp, D. CO_2 emission of Indonesian fires in 2015 estimated from satellite-derived atmospheric CO_2 concentrations. *Geophys. Res. Lett.* **2017**, *44*, 1537–1544. [CrossRef]
16. Buchwitz, M.; Reuter, M.; Schneising, O.; Noël, S.; Gier, B.; Bovensmann, H.; Burrows, J.P.; Boesch, H.; Anand, J.; Parker, R.J.; et al. Computation and analysis of atmospheric carbon dioxide annual mean growth rates from satellite observations during 2003–2016. *Atmos. Chem. Phys.* **2018**, *18*, 17355–17370. [CrossRef]
17. He, Z.; Lei, L.; Welp, L.R.; Zeng, Z.C.; Bie, N.; Yang, S.; Liu, L. Detection of spatiotemporal extreme changes in atmospheric CO_2 concentration based on satellite observations. *Remote Sens.* **2018**, *10*, 839. [CrossRef]
18. Jones, C.D.; Collins, M.; Cox, P.M.; Spall, S.A. The carbon cycle response to ENSO: A coupled climate-carbon cycle model study. *J. Clim.* **2001**, *21*, 4113–4129. [CrossRef]
19. Schimel, D.; Stephens, B.B.; Fisher, J.B. Effect of increasing CO_2 on the terrestrial carbon cycle. *Proc. Natl. Acad. Sci. USA* **2015**, *112*, 436–441. [CrossRef]
20. Kim, J.S.; Kug, J.S.; Yoon, J.H.; Jeong, S.J. Increased atmospheric CO_2 growth rate during El Niño driven by reduced terrestrial productivity in the CMIP5 ESMs. *J. Clim.* **2016**, *29*, 8783–8805. [CrossRef]
21. Liu, J.; Bowman, K.W.; Schimel, D.S.; Parazoo, N.C.; Jiang, Z.; Lee, M.; Bloom, A.A.; Wunch, D.; Frankenberg, C.; Sun, Y.; et al. Contrasting carbon cycle responses of the tropical continents to the 2015–2016 El Niño. *Science* **2017**, *358*, eaam5690. [CrossRef] [PubMed]
22. Chylek, P.; Tans, P.; Christy, P.; Dubey, M.K. The carbon cycle response to two El Nino types: An observational study. *Environ. Res. Lett.* **2018**, *13*, 024001. [CrossRef]
23. Eldering, A.; Wennberg, P.O.; Crisp, D.; Schimel, D.S.; Gunson, M.R.; Chatterjee, A.; Liu, J.; Schwandner, F.M.; Sun, Y.; O'Dell, C.W.; et al. The Orbiting Carbon Observatory-2 early science investigations of regional carbon dioxide fluxes. *Science* **2017**, *358*, eaam5745. [CrossRef]
24. Schneising, O.; Heymann, J.; Buchwitz, M.; Reuter, M.; Bovensmann, H.; Burrows, J. Anthropogenic carbon dioxide source areas observed from space: Assessment of regional enhancements and trends. *Atmos. Chem. Phys.* **2013**, *13*, 2445–2454. [CrossRef]
25. Kort, E.A.; Frankenberg, C.; Miller, C.; Oda, T. Space-based observations of megacity carbon dioxide. *Geophys. Res. Lett.* **2012**, *39*, L17806. [CrossRef]
26. Keppel-Aleks, G.; Wennberg, P.O.; O'Dell, C.W.; Wunch, D. Towards constraints on fossil fuel emissions from total column carbon dioxide. *Atmos. Chem. Phys.* **2013**, *13*, 4349–4357. [CrossRef]
27. Lei, L.P.; Zhong, H.; He, Z.H.; Cai, B.F.; Yang, S.Y.; Wu, C.J.; Zeng, Z.C.; Liu, L.Y.; Zhang, B. Assessment of atmospheric CO_2 concentration enhancement from anthropogenic emissions based on satellite observations. *Chin. Sci. Bull.* **2017**, *62*, 2941–2950. [CrossRef]
28. Schwandner, F.M.; Gunson, M.R.; Miller, C.E.; Carn, S.A.; Eldering, A.; Krings, T.; Verhulst, K.R.; Schimel, D.S.; Nguyen, H.M.; Crisp, D.; et al. Spaceborne detection of localized carbon dioxide sources. *Science* **2017**, *358*, eaam5782. [CrossRef] [PubMed]
29. Shim, C.; Han, J.; Henze, D.; Yoon, T. Identifying local anthropogenic CO_2 emissions with satellite retrievals: A case study in South Korea. *Int. J. Remote Sens.* **2019**, *40*, 1011–1029. [CrossRef]
30. Nassar, R.; Hill, T.G.; McLinden, C.A.; Wunch, D.; Jones, D.B.A.; Crisp, D. Quantifying CO_2 emissions from individual power plants from space. *Geophys. Res. Lett.* **2017**, *44*, 10045–10053. [CrossRef]
31. Wang, S.; Zhang, Y.; Hakkarainen, J.; Ju, W.; Liu, Y.; Jiang, F.; He, W. Distinguishing anthropogenic CO_2 emissions from different energy intensive industrial sources using OCO-2 observations: A case study in northern China. *J. Geophys. Res. Atmos.* **2018**, *123*, 1–12. [CrossRef]
32. Reuter, M.; Buchwitz, M.; Schneising, O.; Krautwurst, S.; O'Dell, C.W.; Richter, A.; Bovensmann, H.; Burrows, J.P. Towards monitoring localized CO_2 emissions from space: Co-located regional CO_2 and NO_2 enhancements observed by the OCO-2 and S5P satellites. *Atmos. Chem. Phys.* **2019**, *19*, 9371–9383. [CrossRef]
33. Wang, J.; Liu, Z.; Zeng, N.; Jiang, F.; Wang, H.; Ju, W. Spaceborne detection of XCO_2 enhancement induced by Australian mega-bushfires. *Environ. Res. Lett.* **2020**, *15*, 124069. [CrossRef]
34. Janardanan, R.; Maksyutov, S.; Oda, T.; Saito, M.; Kaiser, J.W.; Ganshin, A.; Stohl, A.; Matsunaga, T.; Yoshida, Y.; Yokota, T. Comparing GOSAT observations of localized CO_2 enhancements by large emitters with inventory-based estimates. *Geophys. Res. Lett.* **2016**, *43*, 3486–3493. [CrossRef]
35. Hakkarainen, J.; Ialongo, I.; Tamminen, J. Direct space-based observations of anthropogenic CO_2 emission areas from OCO-2. *Geophys. Res. Lett.* **2016**, *43*, 11400–11406. [CrossRef]
36. Hakkarainen, J.; Ialongo, I.; Maksyutov, S.; Crisp, D. Analysis of Four Years of Global XCO_2 Anomalies as Seen by Orbiting Carbon Observatory-2. *Remote Sens.* **2019**, *11*, 850. [CrossRef]

37. Silva, S.J.; Arellano, A.F. Characterizing regional-scale combustion using satellite retrievals of CO, NO_2 and CO_2. *Remote Sens.* **2017**, *9*, 744. [CrossRef]
38. Park, H.; Jeong, S.; Park, H.; Labzovskii, L.D.; Bowman, K.W. An assessment of emission characteristics of Northern Hemisphere cities using spaceborne observations of CO_2, CO, and NO_2. *Remote Sens. Environ.* **2021**, *254*, 112246. [CrossRef]
39. Goddard Earth Science Data Information and Services Center (GES DISC) at National Aeronautics and Space Administration (NASA). Available online: https://oco2.gesdisc.eosdis.nasa.gov/data/ (accessed on 19 January 2021).
40. Zeng, Z.-C.; Lei, L.; Hou, S.; Ru, F.; Guan, X.; Zhang, B. A regional gap-filling method based on spatiotemporal variogram model of columns. *IEEE Trans. Geosci. Remote Sens.* **2014**, *52*, 3594–3603. [CrossRef]
41. Guo, L.J.; Lei, L.P.; Zeng, Z.-C.; Zou, P.F.; Liu, D.; Zhang, B. Evaluation of spatio-temporal variogram models for Mapping XCO_2 using satellite observations: A Case Study in China. *IEEE J. Sel. Top. Appl. Earth Obs. Remote Sens.* **2015**, *8*, 376–385. [CrossRef]
42. Zeng, Z.-C.; Lei, L.; Strong, K.; Jones, D.B.A.; Guo, L.; Liu, M.; Deng, F.; Deutscher, N.M.; Dubey, M.K.; Griffith, D.W.T.; et al. Global land mapping of satellite-observed CO_2 total columns using spatio-temporal geostatistics. *Int. J. Digit. Earth* **2017**, *10*, 426–456. [CrossRef]
43. He, Z.; Lei, L.; Zhang, Y.; Sheng, M.; Wu, C.; Li, L.; Zeng, Z.-C.; Welp, L.R. Spatio-temporal mapping of multi-satellite observed column atmospheric CO_2 using precision-weighted kriging method. *Remote Sens.* **2020**, *12*, 576. [CrossRef]
44. Peters, W.; Jacobson, A.R.; Sweeney, C.; Andrews, A.E.; Conway, T.J.; Masarie, K.; Miller, J.B.; Bruhwiler, L.M.; Petron, G.; Hirsch, A.I.; et al. An atmospheric perspective on North American carbon dioxide exchange: CarbonTracker. *Proc. Natl. Acad. Sci. USA* **2007**, *104*, 18925–18930. [CrossRef]
45. Jacobson, A.R.; Schuldt, K.N.; Miller, J.B.; Oda, T.; Tans, P.; Andrews, A.; Mund, J.; Ott, L.; Collatz, G.J.; Aalto, T.; et al. CarbonTracker CT2019B. NOAA Global Monitoring Laboratory. Available online: https://gml.noaa.gov/ccgg/carbontracker/CT2019B/ (accessed on 13 May 2021).
46. The World Data Centre for Greenhouse Gases (WDCGG). Available online: https://gaw.kishou.go.jp/ (accessed on 28 December 2020).
47. Oda, T.; Maksyutov, S. A very high-resolution (1 km×1 km) global fossil fuel CO_2 emission inventory derived using a point source database and satellite observations of nighttime lights. *Atmos. Chem. Phys.* **2011**, *11*, 543–556. [CrossRef]
48. Oda, T.; Maksyutov, S.; Andres, R.J. The Open-source Data Inventory for Anthropogenic CO_2, version 2016 (ODIAC2016): A global monthly fossil fuel CO_2 gridded emissions data product for tracer transport simulations and surface flux inversions. *Earth Syst. Sci. Data* **2018**, *10*, 87–107. [CrossRef]
49. Tomohiro Oda, Shamil Maksyutov (2015). ODIAC Fossil Fuel CO_2 Emissions Dataset (2020B). Center for Global Environmental Research, National Institute for Environmental Studies, 2020. Available online: https://db.cger.nies.go.jp/dataset/ODIAC/DL_odiac2020b.html (accessed on 29 November 2020). [CrossRef]
50. Ropelewski, C.F.; Jones, P.D. An Extension of the Tahiti–Darwin Southern Oscillation Index. *Mon. Weather. Rev.* **1987**, *115*, 2161–2165. [CrossRef]
51. Southern Oscillation Index (SOI). Available online: http://www.cru.uea.ac.uk/cru/data/soi/ (accessed on 16 June 2021).
52. Oceanic Niño Index (ONI). Available online: https://psl.noaa.gov/data/climateindices/list/ (accessed on 16 June 2021).
53. Keppel-Aleks, G.; Wennberg, P.O.; Schneider, T. Sources of variations in total column carbon dioxide. *Atmos. Chem. Phys.* **2011**, *11*, 3581–3593. [CrossRef]
54. Stewart, R.H. Density, Potential Temperature, and Neutral Density. In *Introduction to Physical Oceanography*; Texas A & M University: College Station, TX, USA, 2008; pp. 83–88.
55. Land Processes Distributed Active Archive Center (LP DAAC). Available online: https://ladsweb.modaps.eosdis.nasa.gov/ (accessed on 24 January 2021).
56. Fan, C.; Li, Z.; Li, Y.; Dong, J.; van der A., R.; de Leeuw, G. Variability of NO_2 concentrations over China and effect on air quality derived from satellite and ground-based observations. *Atmos. Chem. Phys.* **2021**, *21*, 7723–7748. [CrossRef]
57. Sentinel-5P OFFL NO_2: Offline Nitrogen Dioxide. Available online: https://developers.google.com/earth-engine/datasets/catalog/COPERNICUS_S5P_OFFL_L3_NO2 (accessed on 15 February 2021).
58. Sentinel-5P TROPOMI NO_2 Data Products. Available online: http://www.tropomi.eu/data-products/nitrogen-dioxide (accessed on 15 February 2021).
59. Thoning, K.W.; Tans, P.P.; Komhyr, W.D. Atmospheric carbon dioxide at Mauna Loa Observatory: 2. Analysis of the NOAA GMCC data, 1974–1985. *J. Geophys. Res. Atmos.* **1989**, *94*, 8549–8565. [CrossRef]
60. Conway, T.J.; Tans, P.P.; Waterman, L.S.; Thoning, K.W.; Kitzis, D.R.; Masarie, K.A.; Zhang, N. Evidence for interannual variability of the carbon cycle from the National Oceanic and Atmospheric Administration/Climate Monitoring and Diagnostics Laboratory global air sampling network. *J. Geophys. Res.* **1994**, *99*, 22831–22855. [CrossRef]
61. Masarie, K.A.; Tans, P.P. Extension and integration of atmospheric carbon dioxide data into a globally consistent measurement record. *J. Geophys. Res.* **1995**, *100*, 11593–11610. [CrossRef]
62. Wunch, D.; Wennberg, P.O.; Messerschmidt, J.; Parazoo, N.C.; Toon, G.C.; Deutscher, N.M.; Keppel-Aleks, G. The covariation of Northern Hemisphere summertime CO_2 with surface temperature in boreal regions. *Atmos. Chem. Phys.* **2013**, *13*, 9447–9459. [CrossRef]
63. Liu, D.; Lei, L.P.; Guo, L.J.; Zeng, Z.C. A cluster of CO_2 change characteristics with GOSAT observations for viewing the spatial pattern of CO_2 emission and absorption. *Atmosphere* **2015**, *6*, 1695–1713. [CrossRef]

64. van der Werf, G.R.; Randerson, J.T.; Giglio, L.; van Leeuwen, T.T.; Chen, Y.; Rogers, B.M.; Mu, M.; van Marle, M.J.E.; Morton, D.C.; Collatz, G.J.; et al. Global fire emissions estimates during 1997–2016. *Earth Syst. Sci. Data* **2017**, *9*, 697–720. [CrossRef]
65. Le Quéré, C.; Jackson, R.B.; Jones, M.W.; Smith, A.J.P.; Abernethy, S.; Andrew, R.M.; De-Gol, A.J.; Willis, D.R.; Shan, Y.; Canadell, J.G.; et al. Temporary reduction in daily global CO_2 emissions during the COVID-19 forced confinement. *Nat. Clim. Chang.* **2020**, *10*, 647–653. [CrossRef]
66. Buchwitz, M.; Reuter, M.; Nol, S.; Bramstedt, K.; Crisp, D. Can a regional-scale reduction of atmospheric CO_2 during the COVID-19 pandemic be detected from space? A case study for East China using satellite XCO_2 retrievals. *Atmos. Meas. Tech.* **2020**, *14*, 2141–2166. [CrossRef]
67. Zheng, B.; Geng, G.; Ciais, P.; Davis, S.J.; Martin, R.V.; Meng, J.; Wu, N.; Chevallier, F.; Broquet, G.; Boersma, F.; et al. Satellite-based estimates of decline and rebound in China's CO_2 emissions during COVID-19 pandemic. *Sci. Adv.* **2020**, *6*, eabd4998. [CrossRef] [PubMed]
68. Wang, X.; Zhang, R. How did air pollution change during the COVID-19 outbreak in China? *Bull. Am. Meteorol. Soc.* **2020**, *101*, E1645–E1652. [CrossRef]